

# Geophysical Research Letters

## RESEARCH LETTER

10.1029/2020GL087644

### Key Points:

- The CESM1 model frequently simulates a type of reintensified multiyear El Niño events resembling the 2014–2016 extreme El Niño
- The succession and reintensification characteristics of these events are associated with negative phases of the NPO and IOD, respectively
- The phases of NPO and IOD are closely related to the occurrences of reintensified multiyear and transitional single-year El Niño events

### Supporting Information:

- Supporting Information S1

### Correspondence to:

J. -W. Kim,  
jjwok13@uci.edu

### Citation:

Kim, J. -W., & Yu, J. -Y. (2020). Understanding reintensified multiyear El Niño events. *Geophysical Research Letters*, 47, e2020GL087644. <https://doi.org/10.1029/2020GL087644>

Received 24 FEB 2020

Accepted 30 MAY 2020

Accepted article online 4 JUN 2020

## Understanding Reintensified Multiyear El Niño Events

Ji-Won Kim<sup>1</sup>  and Jin-Yi Yu<sup>1</sup> 

<sup>1</sup>Department of Earth System Science, University of California, Irvine, CA, USA

**Abstract** To understand the unique temporal evolution of the 2014–2016 multiyear El Niño event, which can be characterized as a successive and reintensified event preceded by a weak El Niño, this study examines similar events in a 2,200-yr simulation of Community Earth System Model, version 1. By contrasting multiyear El Niño events with single-year ones, we find that the succession characteristics of multiyear El Niño events are primarily caused by a negative North Pacific Oscillation (NPO) in the first-year winter via subtropical Pacific coupling processes. By contrasting reintensified multiyear El Niño events with lingering ones, we find that the reintensification characteristics are caused by a negative Indian Ocean Dipole (IOD) in the first-year fall via tropical interbasin coupling processes. The phase information of the preceding winter NPO and fall IOD together can be used to project the evolution characteristics of El Niño events, particularly the reintensified multiyear and transitional single-year events.

**Plain Language Summary** The 2015–2016 El Niño, categorized as a very strong event like the 1997–1998 and 1982–1983 events, was unique in its evolution in time as it was preceded by a weak El Niño. By analyzing a long-term simulation produced by a state-of-the-art climate model, this study uncovers two key factors driving these types of multiyear El Niño events: a meridional shift of the northern winter Aleutian Low pressure system over the North Pacific (known as the North Pacific Oscillation) and a zonal dipole-like pattern of northern fall sea surface temperatures in the Indian Ocean (known as the Indian Ocean Dipole). This study also explains how these two factors invoke tropical-extratropical interactions in the Pacific and interbasin interactions between the Indian and Pacific Oceans to give rise to the evolution characteristics of these multiyear events. Findings from this study may help improve predictions of multiyear El Niño events.

### 1. Introduction

El Niño events, characterized by anomalous sea surface warming over the central eastern equatorial Pacific Ocean, exert pronounced global impacts extending to land/marine habitats, water availability, food security, economics, and social stability via their global climatic teleconnections (e.g., Barnard et al., 2015; Cashin et al., 2017; Glantz, 2001; Iizumi et al., 2014; Yeh et al., 2018). Since the impacts are usually anticipated to be proportional to the intensities of El Niño events (e.g., Adams et al., 1999), understanding the dynamics of strong or very strong (often called “extreme”) El Niño events is critically important. There has been much research on the latest extreme El Niño event of 2015–2016 which was characteristically distinct from the previous two extreme El Niño events that occurred in 1997–1998 and 1982–1983 (e.g., Kim & An, 2018; Newman et al., 2018; Paek et al., 2017; Ren et al., 2017; Santoso et al., 2017). For example, warm sea surface temperature (SST) anomalies (SSTAs) during the peak of the 2015–2016 event were shifted noticeably to the west compared with the earlier events, resulting in record-breaking warm SSTAs in the central equatorial Pacific. This was unlike the warm SSTAs of the 1997–1998 and 1982–1983 events that peaked in far-eastern equatorial Pacific closer to the South American coast (McPhaden & Zhang, 2009; Santoso et al., 2013).

Aside from these spatially distinct characteristics, the 2015–2016 El Niño also exhibited a different temporal evolution from that of the previous two extreme events. The 2015–2016 extreme El Niño was preceded by a weak El Niño event during 2014 and 2015 (Figure 1). This indicates a possibility that the very strong 2015–2016 El Niño event was part of a multiyear event (simply, the 2014–2016 multiyear El Niño event). In contrast, the 1997–1998 and 1982–1983 extreme El Niño events were both preceded by a La Niña-like condition (i.e., cold SSTAs) in the equatorial Pacific. Thus, they were single-year El Niño events (supporting information Figure S1). Collectively, the 2015–2016 extreme El Niño contains two unique evolution characteristics that were absent in the previous two extreme events: succession and reintensification. Succession

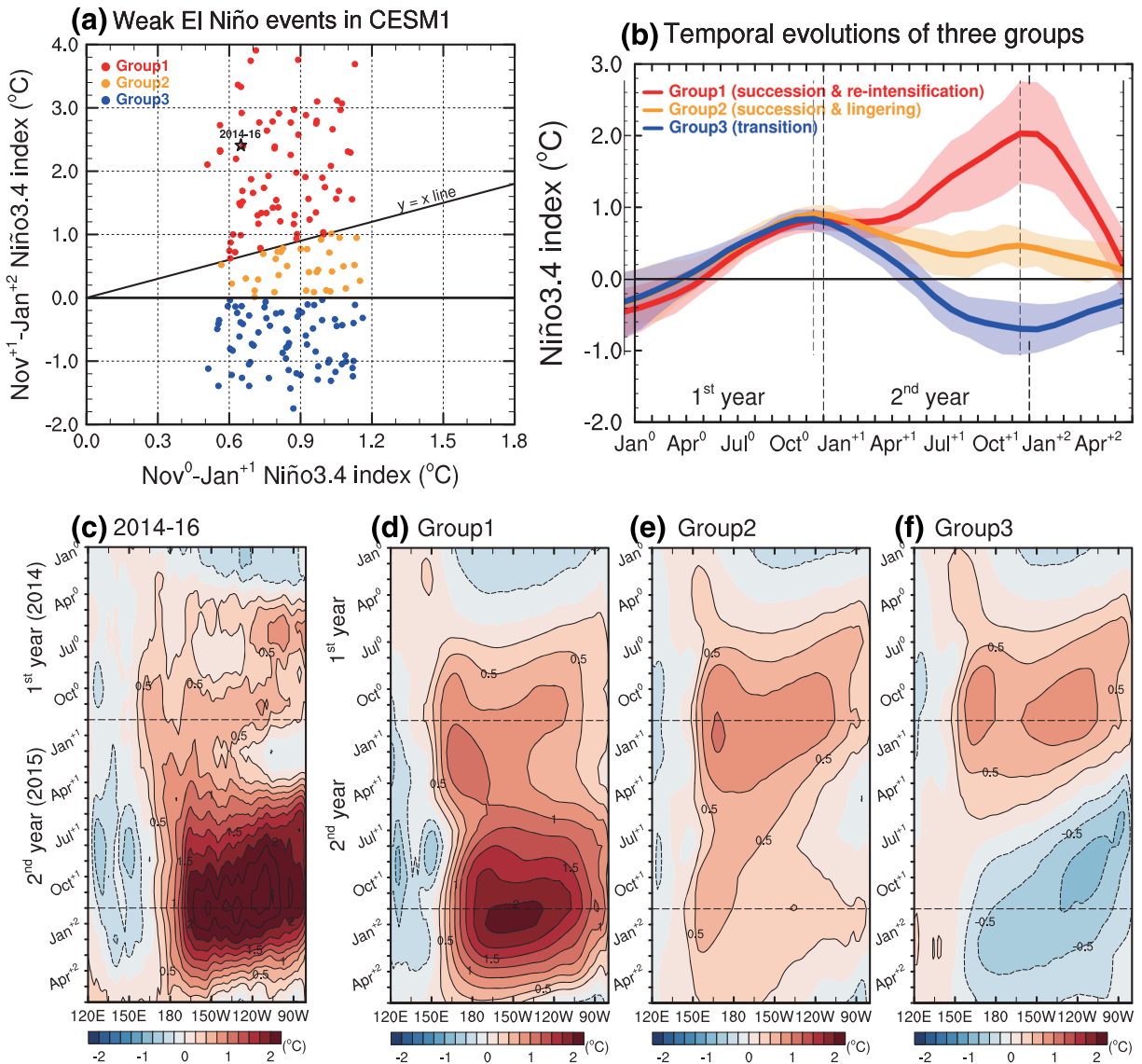


**Figure 1.** (a) Scatter plot of first winter (i.e., November<sup>0</sup>-January<sup>+1</sup>) Niño3.4 index (in °C) against second winter (i.e., November<sup>+1</sup>-January<sup>+2</sup>) Niño3.4 index for the weak El Niño events in CESM1. Red, orange, and blue dots respectively indicate the events classified into Group1, Group2, and Group3 in this study. Note that the 2014-2016 event is marked with a black star. (b) Temporal evolutions of the Niño3.4 index from January<sup>0</sup> to June<sup>+2</sup> for Group1 (red curve), Group2 (orange curve), and Group3 (blue curve). The shadings indicate interquartile ranges between the 25th and 75th percentiles. (c-f) Longitude-time plot of equatorial Pacific SSTAs (in °C) averaged over 5°S to 5°N from January<sup>0</sup> to June<sup>+2</sup> for (c) the 2014-2016 event, (d) Group1, (e) Group2, and (f) Group3.

refers to the fact that the 2015-2016 El Niño was preceded by another 2014-2015 El Niño. Reintensification refers to the fact that the preceding weak El Niño redeveloped into a stronger El Niño in the second year.

The goal of this study is to identify the causes for these evolution characteristics of multiyear El Niño events resembling the 2014-2016 event. Since the number of reintensified multiyear El Niño events is limited in the observations, we here examine similar multiyear El Niño events in a long (i.e., 2,200-yr) simulation from the Community Earth System Model, Version 1 (CESM1; Hurrell et al., 2013; Kay et al., 2015). Previous studies have shown that CESM1 simulates key features of El Niño (also El Niño-Southern Oscillation, ENSO), such as its recurrence frequencies, amplitude ranges, spatial structures, and temporal evolutions (DiNezio et al., 2017; Wu et al., 2019). More importantly, as to be shown later, the CESM1 simulation frequently produces the reintensified multiyear El Niño events that resemble the 2014-2016 event.

## 2. Data and Methods

We analyzed monthly mean SST, sea level pressure (SLP), and surface wind during the model years 400–2,200 of the CESM1 preindustrial simulation, for which the model exhibits a negligible SST trend ( $\sim 10^{-7}^{\circ}\text{C}/100\text{ yr}$ ) and a minor drift of global ocean temperature ( $\sim 0.005^{\circ}\text{C}/100\text{ yr}$ ). For the analyses of the 2014–2016 event, two monthly mean reanalysis data sets were utilized. For the observed SST information, we used the Hadley Center Sea Ice and Sea Surface Temperature (HadISST) data (Rayner et al., 2003). For the observed information of SLP and surface wind, we used the National Center for Environmental Prediction/National Center for Atmospheric Research (NCEP/NCAR) Reanalysis 1 data (Kalnay et al., 1996).

We identified weak El Niño events in the CESM1 simulation based on the values of the Niño3.4 index (i.e., SSTAs averaged in  $5^{\circ}\text{S}$  to  $5^{\circ}\text{N}$  and  $170^{\circ}\text{W}$ – $120^{\circ}\text{W}$ ). An El Niño event was determined to be a weak event when its December Niño3.4 index is greater than 0.5 but less than 1.0 standard deviation (s.d.). The months of the year when the weak El Niño develops were denoted January<sup>0</sup>, February<sup>0</sup>, ..., and December<sup>0</sup>. The months of the year following the weak El Niño were denoted as January<sup>+1</sup>, February<sup>+1</sup>, ..., and December<sup>+1</sup>, and so on for the next year. Two other climate indices were also used in the analysis: the North Pacific Oscillation (NPO; Rogers, 1981) index and the Indian Ocean Dipole (IOD; Saji et al., 1999) index. The NPO index which represents the north-south seesaw in winter SLP variations over the North Pacific is defined by the principal component (PC) corresponding to the second empirical orthogonal function (EOF) mode of normalized SLP anomalies over the North Pacific ( $20^{\circ}\text{N}$ – $60^{\circ}\text{N}$  and  $120^{\circ}\text{E}$  to  $80^{\circ}\text{W}$ ) during extended winter (i.e., November–March). The IOD index represents the Indian Ocean dipole/zonal mode. It is defined as the normalized SSTA difference between the western Indian Ocean ( $10^{\circ}\text{S}$  to  $10^{\circ}\text{N}$  and  $50^{\circ}\text{E}$ – $70^{\circ}\text{E}$ ) and the southeastern Indian Ocean ( $10^{\circ}\text{S}$  to the equator and  $90^{\circ}\text{E}$ – $110^{\circ}\text{E}$ ) during extended fall (i.e., July–November), in which IOD events usually develop and peak (cf. Saji et al., 1999). Note that all the seasons used here are for the Northern Hemisphere.

Anomalies were defined as departures from monthly climatology for the entire analysis period (i.e., model year 400–2,200 for CESM1 and year 1958–2018 for the reanalysis data sets) after removing their linear trends. A number of statistical analysis methods such as composite and regression analyses were applied to diagnose the anomalies. An interquartile range between the 25th and 75th percentiles was employed to describe the values of the middle 50% in the scatter and evolution pattern plots.

## 3. Results

### 3.1. Grouping Weak El Niño Events

We first categorized weak El Niño events in the CESM1 simulation into three groups according to their evolution characteristics (Figure 1a). The first group (Group1) consists of events that occur when the winter Niño3.4 index during the second year (i.e., November<sup>+1</sup>–January<sup>+2</sup>) is larger than that during the first year (i.e., November<sup>0</sup>–January<sup>+1</sup>). This group is considered as reintensified multiyear El Niño events that have the succession and reintensification characteristics (red dots lying above the  $y = x$  line in Figure 1a). The second group (Group2) is defined as events that occur when the Niño3.4 index of the second winter is smaller than that of the first winter but remains positive. This group is considered as lingering events (orange dots lying below the  $y = x$  line), meaning that they are also multiyear El Niño events (including the succession characteristics) but without a reintensification during the second year. The remaining events, which have transitioned to a La Niña-like condition in the second year, are referred to as Group3. This group is considered as transitional single-year events (blue dots in Figure 1a). Around 60% of the weak El Niño events in CESM1 have the succession characteristics (a total of 106 events from Group1 and Group2; see Table S1). Those results are rather similar to observational results, which indicate that weaker El Niño events have a tendency to produce a larger number of successive events in comparison to stronger El Niño events that generally have transition events in the second year (e.g., Horii & Hanawa, 2004). It should also be noted that CESM1 simulates a large number of reintensified multiyear events (73 events in Group1, 41% of all weak El Niño events; see Table S1); thus, it provides a large sample size to study the causes for the succession and reintensification characteristics of weak El Niño events.

To confirm our classification method, we plot the temporal evolutions of the Niño3.4 index for all the three groups from January<sup>0</sup> to June<sup>+2</sup> (Figure 1b). The three groups show similar evolutions during the first year where the weak El Niño events develop and reach their peak intensities in the winter. The evolutions become different among the three groups after the spring of the second year as follows: (i) Group1 grows to a second and stronger peak that decays abruptly afterward (red curve); (ii) Group2 exhibits a stable lingering that eventually decays (orange curve); and (iii) Group3 experiences a fast transition to a La Niña condition with subsequent slow decay (blue curve). The 25th and 75th percentile interquartile ranges from the three groups (colored shadings) reveal that these evolution differences are statistically significant.

The longitude-time plots displayed in Figures 1d–1f further illustrate how the weak El Niño events in the three groups evolve differently over the equatorial Pacific. For Group1 (Figure 1d), the central equatorial Pacific warm SSTAs in the first winter (i.e., the first-year weak El Niño) persist into spring of the second year and then subsequently extend to the east, covering the central eastern equatorial Pacific. These warm SSTAs then grow rapidly, eventually producing the stronger second-year El Niño. For Group2 (Figure 1e), the first winter warm SSTAs in the central equatorial Pacific also persist into the next spring and extend thereafter. However, these warm SSTAs do not grow in the following seasons, instead lingering and slowly decaying in the second year. For Group3 (Figure 1f), the warm SSTAs in the central equatorial Pacific continually decay after their peak during the first winter. They transition into La Niña-like conditions with cold anomalies originating from far-eastern equatorial Pacific, propagating to the west and covering the entire equatorial Pacific during the following seasons in the second year.

The 2014–2016 event, which should be categorized as a Group1 event based on our classification method (see the star in Figure 1a), generally follows Group1's evolution characteristics (cf. Figures 1c and 1d). Minor discrepancies exist between this observed event and the Group1 events simulated in CESM1, which include (i) a faster growth rate during the second year for the observed event than the simulated events (0.21°C/month for the 2014–2016 event vs., on average, 0.15°C/month for Group1; cf. the growth rates were computed by a change in SSTAs over the Niño3.4 region during April<sup>+1</sup>–December<sup>+1</sup>) and (ii) a stronger westward propagation of positive SSTAs after the spring of second year for the 2014–2016 event than the Group1 events. Despite these minor discrepancies, the results presented in Figure 1 clearly demonstrate that the 2014–2016 multiyear El Niño event is very similar to the Group1's reintensified multiyear El Niño events that frequently occur in the 2,200-yr CESM1 simulation.

### 3.2. Cause for the Succession Characteristics

To understand the succession characteristics, we contrast the multiyear events in Group1 and Group2 (hereafter, Group1+2) with the single-year events in Group3. The anomalous atmospheric circulation patterns for Group1+2 and Group3 during the extended winter (i.e., November<sup>0</sup>–March<sup>+1</sup>), when the significant evolution changes between the groups have not yet appeared, give us a vital clue as to what is responsible for driving an El Niño-like condition in the year after a weak El Niño event peaks. As compared to Group3, it is evident in Group1+2 that the winter Aleutian Low over the North Pacific, which is usually enhanced by atmospheric teleconnection associated with El Niño, is shifted more southeastward of its climatological location, toward Baja California (Figure 2a vs. Figure 2b). The difference between Group1+2 and Group3 (Figure 2c) confirms this meridional shift in that it exhibits a north-south dipole-like structure in SLP anomalies centered around 150°W. This meridional SLP anomaly structure is highly reminiscent of the negative phase of the NPO (cf. Linkin & Nigam, 2008). The atmospheric pattern obtained by regressing the extended winter SLP and wind anomalies onto the inverse NPO index (Figure 2d) has a strong resemblance to that of this difference map.

The above results collectively suggest that a negative NPO is a crucial cause of driving the succession of first-year weak El Niño events. The scatter plot (Figure 2e) of the first winter Niño3.4 index against the extended winter NPO index for the three groups further supports this suggestion. The weak El Niño events of Group1 and Group2, on average, both have a negative NPO with a stronger negative NPO index in the former (−0.64) and a weaker negative one in the latter (−0.32) (Figure 2e and Table S1). However, Group3's weak El Niño events do not show any preference for a particular phase of the NPO, having an average value of the NPO index close to 0 (−0.04) (Figure 2e and Table S1). Since there is no correlation between the amplitude of weak El Niño events and the intensity of NPO ( $r = 0.06$ ), the NPO (or NPO index) used here could be an independent factor as it has been previously recognized as an intrinsic winter mode of

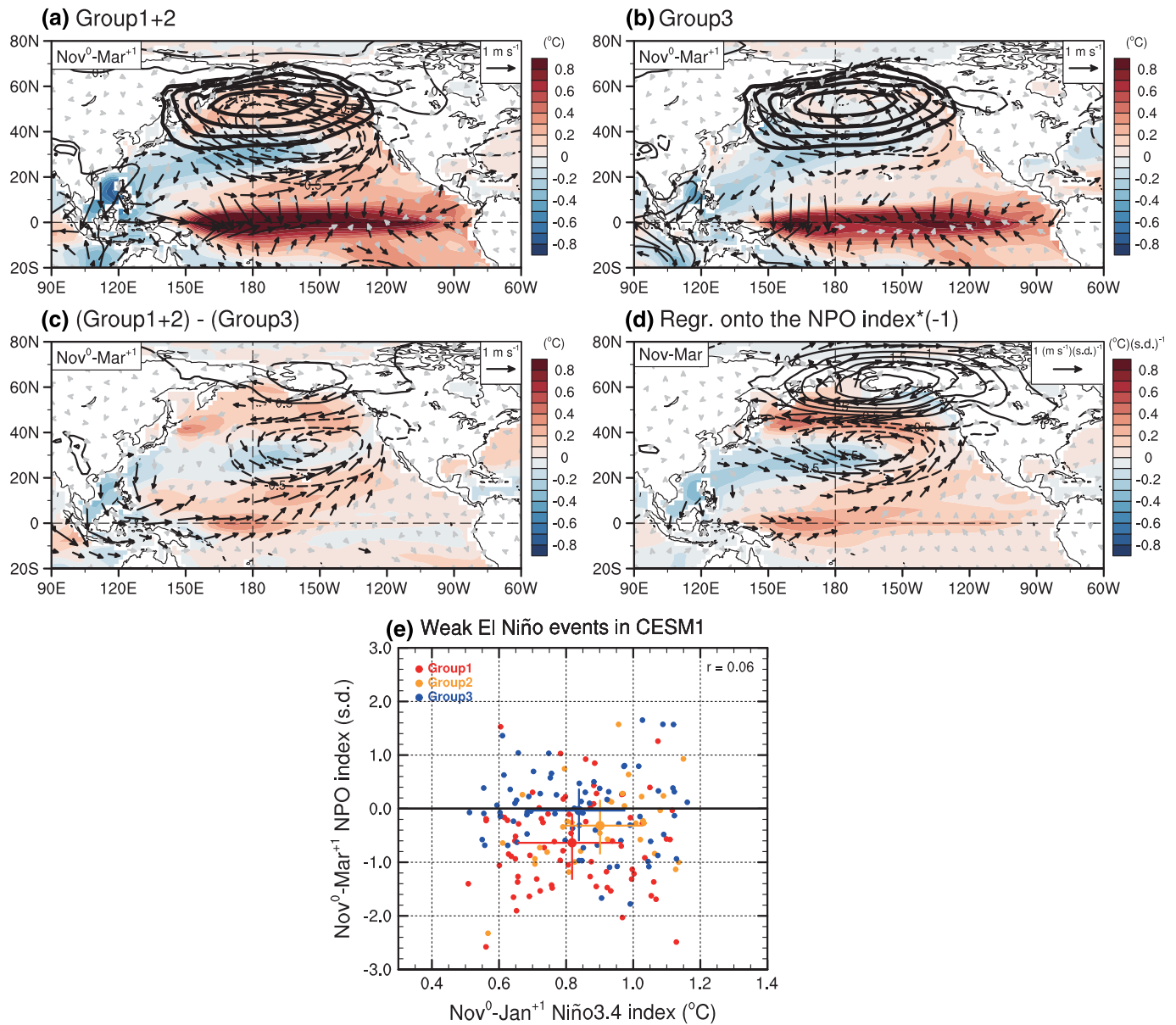


**Figure 2.** Composite map of anomalous SST (shadings; in °C), SLP (contours; in hPa), and surface wind (vectors; in  $\text{m s}^{-1}$ ) during November<sup>0</sup>–March<sup>+1</sup> for (a) Group1+2, (b) Group3, and (c) their difference (i.e., Group1+2 minus Group3). Thick black contours in (a) and (b) indicate the climatological location of the winter Aleutian Low, which is depicted by raw SLP levels from 1,002 to 1,014 hPa (4-hPa interval). (d) Regression map on the inverted NPO index (multiplied by  $-1$ ; in s.d.) using the extended winter anomalous SST (shadings), SLP (contours), and surface wind (vectors). The surface winds in (a)–(d) are expressed as black vectors when their magnitudes are greater than  $0.4 \text{ m s}^{-1}$  (all other vectors are shown in gray). (e) Scatter plot of first winter Niño3.4 index (in °C) against extended winter NPO index (in s.d.) for the weak El Niño events of Group1 (red dots), Group2 (orange dots), and Group3 (blue dots). For each of the three groups, mean values are expressed with thicker dots, and vertical and horizontal lines indicate interquartile ranges between the 25th and 75th percentiles. The correlation coefficient ( $r$ ) between the Niño3.4 and NPO indices is given in the upper right corner.

midlatitude atmospheric variability (Alexander et al., 2010). In other words, when a negative NPO occurs for whatever reasons during the peak winter of a weak El Niño event, the event is more likely to develop a successive equatorial Pacific warming in the following year and become a multiyear El Niño. Previous studies have shown that the negative NPO can induce warm SSTAs in the subtropical Pacific and activate a wind-evaporation-SST (WES) feedback (Xie & Philander, 1994) to spread the warm SSTAs into the equatorial Pacific in the subsequent seasons (e.g., Anderson et al., 2013; Vimont, 2010; Yu & Fang, 2018; Yu & Kim, 2011; Yu et al., 2010; cf. Figure S2).

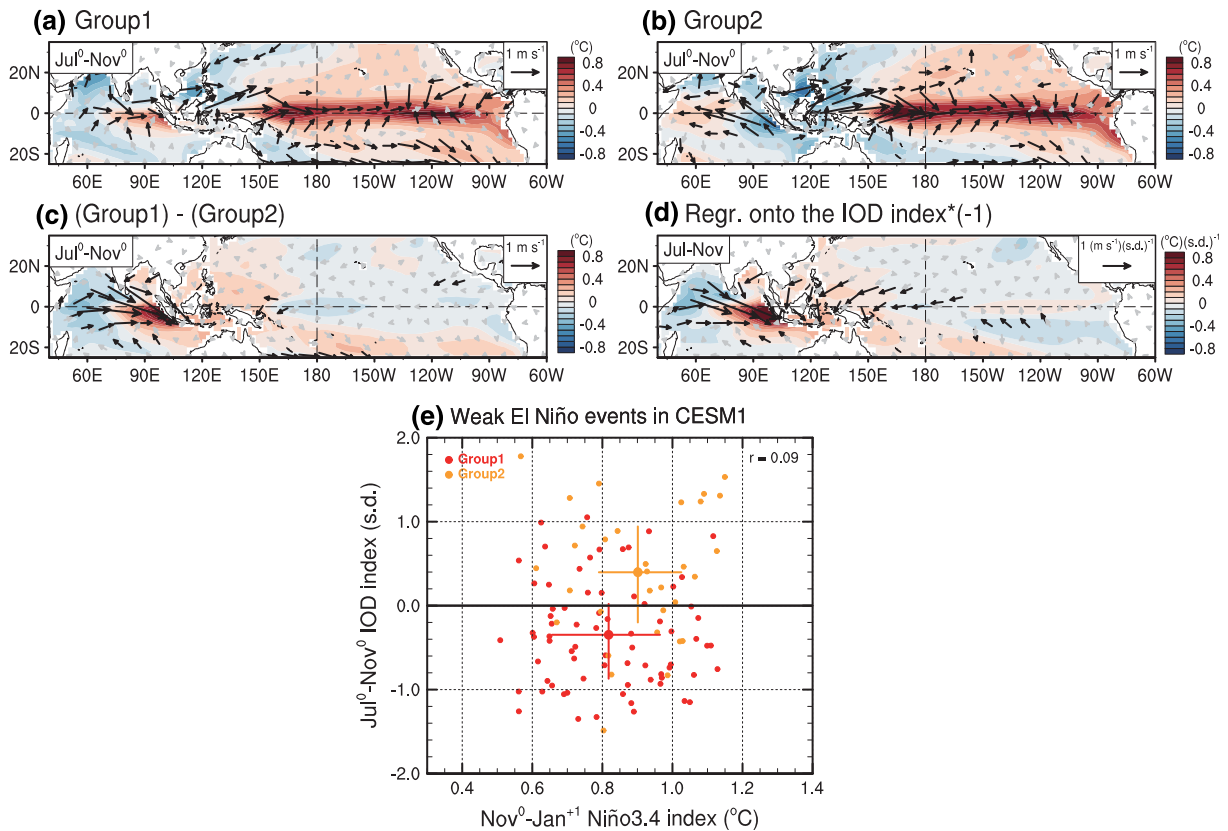


**Figure 3.** Composite map of anomalous SST (shadings; in  $^{\circ}\text{C}$ ) and surface wind (vectors; in  $\text{m s}^{-1}$ ) during July<sup>0</sup>–November<sup>0</sup> for (a) Group1, (b) Group2, and (c) their difference (i.e., Group1 minus Group2). (d) Regression map on the inversed IOD index (multiplied by  $-1$ ; in s.d.) using the extended fall (i.e., July–November) anomalous SST (shadings) and surface wind (vectors). The surface winds in (a)–(d) are expressed as black vectors when their magnitudes are greater than  $0.4 \text{ m s}^{-1}$  (all other vectors are shown in gray). In (d), the impact of ENSO has been excluded by removing the linear regression with respect to the Niño3.4 index. (e) Scatter plot of first winter Niño3.4 index (in  $^{\circ}\text{C}$ ) against preceding extended fall IOD index (in s.d.) for the weak El Niño events of Group1 (red dots) and Group2 (orange dots). For each of the two groups, mean values are expressed with thicker dots, and vertical and horizontal lines indicate interquartile ranges between the 25th and 75th percentiles. The correlation coefficient ( $r$ ) between the Niño3.4 and IOD indices is given in the upper right corner.

### 3.3. Cause for the Reintensification Characteristics

To understand the reintensification characteristics, we contrast the multiyear events in Group1 with those in Group2 since the only difference between the two groups is that the former (latter) has its first-year El Niño intensity reintensified (lingering) during its second year (cf. Figure 1). We find that these two groups are most different in their SSTAs over the Indian Ocean during the extended fall of the first year (i.e., July<sup>0</sup>–November<sup>0</sup>). The SSTAs in Group1 are generally characterized by warm anomalies in the eastern Indian Ocean and cold anomalies in the western Indian Ocean which are accompanied by surface westerly wind anomalies in between (Figure 3a). This zonal dipole SSTa structure closely resembles a negative phase of the IOD (cf. Saji et al., 1999; Webster et al., 1999). In stark contrast to Group1, the Indian Ocean SSTAs in Group2 reveal a positive phase of the IOD (Figure 3a vs. Figure 3b). The difference between Group1 and Group2 (Figure 3c) clearly shows a zonal contrast over the Indian Ocean that enhances the negative IOD-related air-sea structures. The inversed IOD index-regressed map of SST and wind anomalies during fall further supports this (Figure 3d). Figure 3c also illustrates that the differences in the Pacific Ocean are relatively small when compared to those in the Indian Ocean. These results indicate that the phase of the IOD during the first-year fall (when a weak El Niño develops) can affect whether a multiyear El Niño can be reintensified (i.e., Group1) or lingering (i.e., Group2) during its second year. The scatter plot of the first winter Niño3.4 index against the first-year fall IOD index for Group1 and Group2 verifies this idea (Figure 3e). Most weak El Niño events in Group1 co-occur with a negative IOD (54 out of 73 events; occupying 74%) with an average IOD index value of  $-0.35$  (Figure 3e and Table S1). However, around two thirds of the weak El

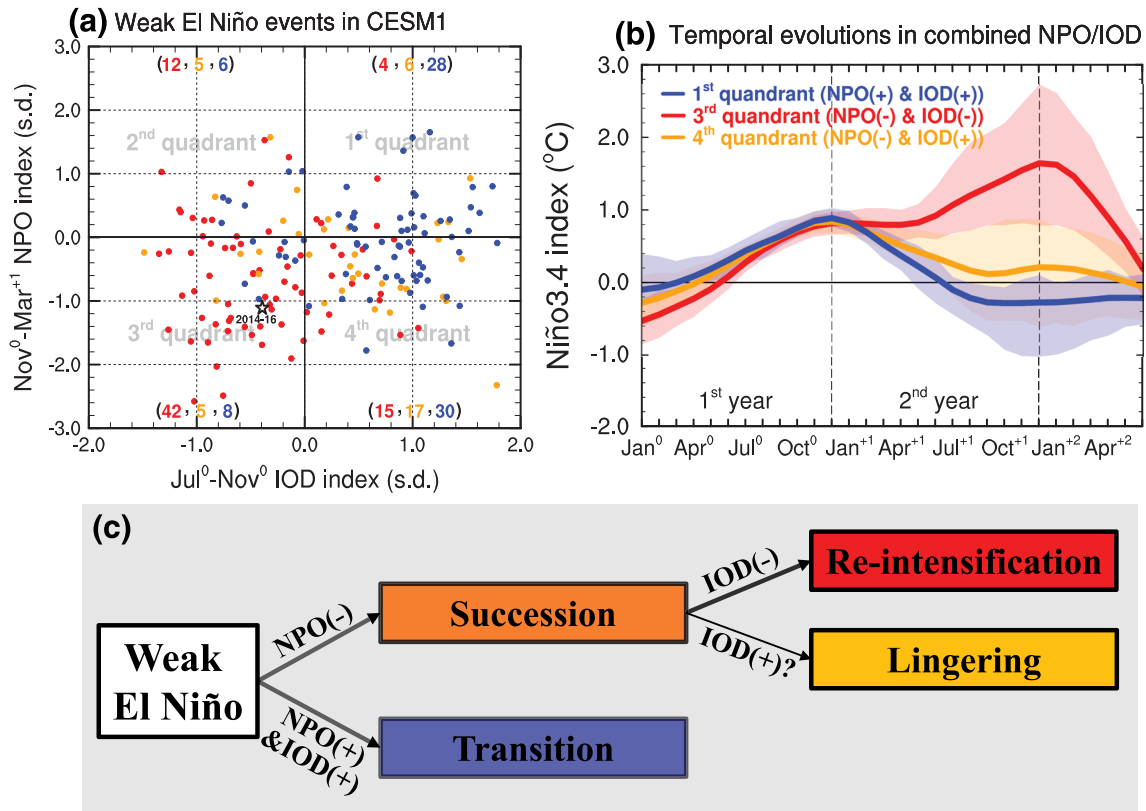


**Figure 4.** (a) Scatter plot of the extended fall (i.e., July<sup>0</sup>-November<sup>0</sup>) IOD index (in s.d.) against the extended winter (i.e., November<sup>0</sup>-March<sup>+1</sup>) NPO index (in s.d.) for the weak El Niño events of Group1 (red dots), Group2 (orange dots), and Group3 (blue dots). The 2014–2016 event is marked with a black star. The numbers of events in each quadrant are shown for the results obtained from Group1, Group2, and Group3 as red, orange, and blue text, respectively. (b) Temporal evolutions of the Niño3.4 index (in °C) from January<sup>0</sup> to June<sup>+2</sup> for the events in the first quadrant (blue curve), third quadrant (red curve), and fourth quadrant (orange curve) from (a). The shadings indicate interquartile ranges between the 25th and 75th percentiles. (c) Schematic diagram describing the second-year evolution characteristics of weak El Niño events controlled by various phase combinations of NPO and IOD based on the findings of this study.

Niño events in Group2 co-occur with a positive IOD (23 out of 33 events; occupying 70%) with an average IOD index value of 0.40 (Figure 3e and Table S1).

Previous research (Izumo et al., 2010, 2016) has shown that a negative IOD can contribute to the development of warm SSTAs in the equatorial Pacific during the next year via the following processes. A negative IOD during fall can enhance easterly anomalies over the Pacific Ocean and westerly anomalies over the Indian Ocean (see Figures 3c and 3d), building up warm subsurface water in the western Pacific. As the time passes, the peaked negative IOD quickly recedes and is replaced by a basin-wide cooling over the Indian Ocean during the following winter and spring (e.g., An, 2004; Yu & Lau, 2005; cf. Figure S3). The basin-wide cooling decreases rainfall/convective heating over the Indian Ocean and then induces an atmospheric Kelvin wave that reverses the easterly anomalies over the western Pacific to westerly anomalies (e.g., Annamalai et al., 2005; Dayan et al., 2015; Kim & An, 2019; Ohba & Ueda, 2007; Watanabe & Jin, 2002; cf. Figure S3). The westerly anomalies can spread the anomalous subsurface warm water from the western Pacific to the east in the form of downwelling oceanic Kelvin waves and lead to the development of warm SSTAs in the central to eastern Pacific during the following summer and winter. Through these tropical coupling processes between the Indian and Pacific Oceans, a negative (positive) IOD during fall can enhance warm (cold) SSTAs over the equatorial Pacific in the following year (see also Cai et al., 2019, for an extensive review of interbasin interaction mechanisms).

It is important to remember that both Group1 and Group2 events are also accompanied by a negative NPO that contributes to maintain the warm anomalies in the equatorial Pacific during the second year via the subtropical Pacific coupling processes (see section 3.2). As a result, the negative IOD in the Group1 events works

together with the negative NPO to reintensify the El Niño events during their second-year evolutions, while the positive IOD in the Group2 events cancels the effects of the negative NPO to hinder the events from reintensifying during their second-year evolutions—resulting in lingering multiyear El Niño events (cf. Figures 1 and S4). Like the NPO, the intensity of the IOD can be independent from the amplitude of weak El Niño events ( $r = 0.09$ ; cf. Figure 3e). Previous studies have conducted numerical experiments demonstrating these influences of NPO and IOD on ENSO evolution (e.g., Alexander et al., 2010; Izumo et al., 2010).

#### 3.4. Evolution Paths of Weak El Niño Events Controlled by Various Phase Combinations of NPO and IOD

Our findings suggest that the phase information of NPO and IOD can be useful to project the evolution characteristics of weak El Niño events. This possibility is explored in Figure 4a, which displays a scatter plot of the extended fall IOD index against the extended winter NPO index for the three groups. Based on the number of events from each of the group in all four quadrants, we find that NPO and IOD phases are most useful in projecting the occurrences of Group1 and Group3 events. Most events in the third quadrant (a negative NPO combined with a negative IOD) are the Group1 events (i.e., 76% of the dots in the third quadrant), whereas most of those in the first quadrant (a positive NPO combined with a positive IOD) are the Group3 events (i.e., 74% of the dots in the first quadrant). Events in the second or fourth quadrant are not utterly dominated by any of the three groups. Nevertheless, consistent with our findings, more than half of the Group2 events lie in the fourth quadrant where a negative NPO combines with a positive IOD. As can be inferred from Figure S5, a positive IOD eventually leads to easterly anomalies over the western Pacific, thereby promoting a phase transition from El Niño to La Niña. However, the negative NPO following the positive IOD would hinder the IOD's transition effect as it can induce opposite westerly anomalies over the western Pacific. Due to this canceling effect, the Group2 events are mostly in the fourth quadrant. The Group3 events also appear frequently in this quadrant (~50%), which is also consistent with our suggestion that a positive IOD favors a phase transition of weak El Niño events in the following year (see section 3.3). On one hand, there are not many events in the second quadrant where a positive NPO combines with a negative IOD. We conclude from these results that when the preceding winter NPO and fall IOD are in the same phases, they can be very good predictors of the occurrence of reintensified multiyear and transitional single-year El Niño events.

Armed with the information above, we plot the temporal evolution of the Niño3.4 index for the first, third, and fourth quadrants (Figure 4b). For the sake of simplicity, the evolution of the limited number of events in the second quadrant is not shown here but can be found in Figure S6. It is easily seen from Figure 4b that there are no significant differences (among the composites from the three quadrants) during the first year through the time the weak El Niño events reach their first peaks. However, significant differences appear afterward. When both the NPO and IOD are in their negative phases (third quadrant; red curve), the El Niño warming is sustained and reintensified after the spring of the second year. This corresponds to the evolution pattern of Group1 events (cf. Figure 1b). When both the NPO and IOD are in their positive phases (first quadrant; blue curve), the El Niño warming decays rapidly and transitions to a cooling phase after the summer of second year and onward. This evolution pattern corresponds to that of Group3 events (cf. Figure 1b). Meanwhile, the evolution pattern from the combination of a negative NPO and a positive IOD (fourth quadrant; orange curve) contains the lingering characteristics that corresponds to the evolution pattern of Group2 events (cf. Figure 1b), but this is a consequence of the mix of half succession events and half transition events as revealed in Figure 4a. The schematic diagram (Figure 4c) summarizes our findings on how the evolution paths of weak El Niño events are controlled by the various phase combinations of the NPO and IOD.

There may be debate on how the rapid reintensification was possible in year 2015 (i.e., the second year of the 2014–2016 event) although the preceding fall IOD was weakly negative ( $-0.39$ ; the star in Figure 4a). Possible reasons for the rapid reintensification could be the strong negative NPO during the extended winter of 2014–2015 ( $-1.10$ ), the head start of the recharged heat content anomaly in the upper equatorial Pacific due to the easterly wind burst during the summer of 2014 (Hu & Fedorov, 2016; Levine & McPhaden, 2016), and the multiyear episode of warm SSTAs in the northeastern Pacific that developed from late 2013 to 2015 (known as “the Blob”; Tseng et al., 2017).

#### 4. Concluding Remarks

Using a large sample size of El Niño events from a long-term CESM1 simulation, we investigated weak El Niño events in order to better understand the evolution characteristics of multiyear El Niño events resembling those of 2014–2016 (i.e., the reintensified multiyear El Niño event, whose evolution pattern is characterized as succession and reintensification). The main finding of this study is that there are two crucial factors responsible for driving the evolution characteristics of reintensified multiyear El Niño events. First, a negative NPO during the winter when a first-year weak El Niño peaks is responsible for the successive evolution of El Niño into the second year. Second, a co-occurrence of a negative IOD during fall (when a first-year weak El Niño develops) with the negative NPO in the following winter is responsible for the reintensification of El Niño in the second year. Our results indicate a possibility of predicting the second-year evolution paths of weak El Niño events by examining the phase combinations of the NPO and IOD.

In order to determine whether our findings can be reproduced using other model simulations, the analyses were repeated using a 1,300-year preindustrial simulation of the NCAR's Community Climate System Model, version 4 (CCSM4; Gent et al., 2011). The results produced (Figures S7 to S9) are in general similar to those produced using the CESM1 (Figures 1–3) (see Text S1 for details). This indicates that our findings are likely not model dependent. We also note that the CESM1 historical simulation produces similar results (not shown). This implies that the findings reported here can also be applied to the historical period.

Besides the 2014–2016 event, only two other reintensified multiyear El Niños (1976–1978 and 1986–1988 events) occurred during the analysis period (Figure S10a). We find that a negative NPO occurred during the first-year winter of the 1976–1978 event and a negative IOD occurred during the first-year summer to fall of the 1986–1988 event (Figures S10b and S10c). Both a negative NPO and a negative IOD occurred during the first year of the 2014–2016 event. This is generally consistent with our suggestion that both a negative NPO and a negative IOD contribute to producing the multiyear feature and their combined effects contribute to the reintensification feature. In this regard, we note that the reintensification is much weaker during the 1976–1978 and 1986–1988 events compared to the 2014–2016 event. The reintensification ratio (maximum value of Niño3.4 index in the second year divided by that in the first year) is 3.72 for the 2014–2016 event but only 1.21 and 1.37 for the 1976–1978 and 1986–1988 events, respectively. Overall, the 1976–1978 and 1986–1988 events are not that similar to the 2014–2016 event. These event-to-event differences have to be eliminated via large sample sizes to reveal the common properties of reintensification events. Since the observations have only a limited number of events, they cannot be of much help for this purpose. Instead, long-term model simulations, such as those examined in the present study, are a useful way to understand the underlying dynamics of reintensified multiyear El Niño events.

Finally, factors other than the atmospheric processes associated with the NPO and the IOD may also contribute to the generation of the reintensified multiyear El Niño events. One such oceanic process is the slow oceanic adjustment related to the wind-driven delayed thermocline feedback (cf. An & Kim, 2017; Jin, 1997). An in-depth analysis capable of shedding light on these detailed dynamics should be undertaken in future studies.

#### Data Availability Statement

The 2,200-yr CESM1 preindustrial simulation was conducted by the CESM project team and are available via the Earth System Grid (<https://www.earthsystemgrid.org/>). The HadISST data were downloaded from the Met Office Hadley Center (<https://www.metoffice.gov.uk/hadobs/>). The NCEP/NCAR Reanalysis 1 data were obtained from their website (<https://www.esrl.noaa.gov/psd/data/gridded/data.ncep.reanalysis.html>).

#### Acknowledgments

We thank Dr. Wenju Cai and an anonymous reviewer for their valuable comments. This research is supported by NSF Climate and Large-Scale Dynamics Program under Grant AGS-1833075. The authors are grateful to all data providers.

#### References

- Adams, R. M., Chen, C. C., McCarl, B. A., & Weiher, R. F. (1999). The economic consequences of ENSO events for agriculture. *Climate Research*, 13(3), 165–172. <https://doi.org/10.3354/cr013165>
- Alexander, M. A., Vimont, D. J., Chang, P., & Scott, J. D. (2010). The impact of extratropical atmospheric variability on ENSO: Testing the seasonal footprinting mechanism using coupled model experiments. *Journal of Climate*, 23(11), 2885–2901. <https://doi.org/10.1175/2010JCLI3205.1>
- An, S. I. (2004). A dynamic link between the basin-scale and zonal modes in the tropical Indian Ocean. *Theoretical and Applied Climatology*, 78(4), 203–215. <https://doi.org/10.1007/s00704-003-0027-2>
- An, S. I., & Kim, J. W. (2017). Role of nonlinear ocean dynamic response to wind on the asymmetrical transition of El Niño and La Niña. *Geophysical Research Letters*, 44, 393–400. <https://doi.org/10.1002/2016GL071971>

- Anderson, B. T., Perez, R. C., & Karspeck, A. (2013). Triggering of El Niño onset through trade wind-induced charging of the equatorial Pacific. *Geophysical Research Letters*, *40*, 1212–1216. <https://doi.org/10.1002/grl.50200>
- Annamalai, H. S. P. X., Xie, S. P., McCreary, J. P., & Murtugudde, R. (2005). Impact of Indian Ocean sea surface temperature on developing El Niño. *Journal of Climate*, *18*(2), 302–319. <https://doi.org/10.1175/JCLI-3268.1>
- Barnard, P. L., Short, A. D., Harley, M. D., Splinter, K. D., Vitousek, S., Turner, I. L., et al. (2015). Coastal vulnerability across the Pacific dominated by El Niño/Southern Oscillation. *Nature Geoscience*, *8*(10), 801–807. <https://doi.org/10.1038/ngeo2539>
- Cai, W., Wu, L., Lengaigne, M., Li, T., McGregor, S., Kug, J. S., et al. (2019). Pantropical climate interactions. *Science*, *363*, eaav4236. <https://doi.org/10.1126/science.aav4236>
- Cashin, P., Mohaddes, K., & Raissi, M. (2017). Fair weather or foul? The macroeconomic effects of El Niño. *Journal of International Economics*, *106*, 37–54. <https://doi.org/10.1016/j.jinteco.2017.01.010>
- Dayan, H., Izumo, T., Vialard, J., Lengaigne, M., & Masson, S. (2015). Do regions outside the tropical Pacific influence ENSO through atmospheric teleconnections? *Climate Dynamics*, *45*(3–4), 583–601. <https://doi.org/10.1007/s00382-014-2254-x>
- DiNezio, P. N., Deser, C., Okumura, Y., & Karspeck, A. (2017). Predictability of 2-year La Niña events in a coupled general circulation model. *Climate Dynamics*, *49*(11–12), 4237–4261. <https://doi.org/10.1007/s00382-017-3575-3>
- Gent, P. R., Danabasoglu, G., Donner, L. J., Holland, M. M., Hunke, E. C., Jayne, S. R., et al. (2011). The community climate system model version 4. *Journal of Climate*, *24*(19), 4973–4991. <https://doi.org/10.1175/2011JCLI4083.1>
- Glantz, M. H. (2001). *Currents of change: Impacts of El Niño and La Niña on climate and society*. Cambridge: Cambridge University Press.
- Horii, T., & Hanawa, K. (2004). A relationship between timing of El Niño onset and subsequent evolution. *Geophysical Research Letters*, *31*, L06304. <https://doi.org/10.1029/2003GL019239>
- Hu, S., & Fedorov, A. V. (2016). Exceptionally strong easterly wind burst stalling El Niño of 2014. *Proceedings of the National Academy of Sciences*, *113*(8), 2005–2010. <https://doi.org/10.1073/pnas.1514182113>
- Hurrell, J. W., Holland, M. M., Gent, P. R., Ghan, S., Kay, J. E., Kushner, P. J., et al. (2013). The community Earth system model: A framework for collaborative research. *Bulletin of the American Meteorological Society*, *94*(9), 1339–1360. <https://doi.org/10.1175/BAMS-D-12-00121.1>
- Iizumi, T., Luo, J. J., Challinor, A. J., Sakurai, G., Yokozawa, M., Sakuma, H., et al. (2014). Impacts of El Niño Southern Oscillation on the global yields of major crops. *Nature Communications*, *5*(1), 3712. <https://doi.org/10.1038/ncomms4712>
- Izumo, T., Vialard, J., Dayan, H., Lengaigne, M., & Suresh, I. (2016). A simple estimation of equatorial Pacific response from windstress to untangle Indian Ocean Dipole and basin influences on El Niño. *Climate Dynamics*, *46*(7–8), 2247–2268. <https://doi.org/10.1007/s00382-015-2700-4>
- Izumo, T., Vialard, J., Lengaigne, M., de Boyer Montegut, C., Behera, S. K., Luo, J. J., et al. (2010). Influence of the state of the Indian Ocean Dipole on the following year's El Niño. *Nature Geoscience*, *3*(3), 168–172. <https://doi.org/10.1038/ngeo760>
- Jin, F. F. (1997). An equatorial ocean recharge paradigm for ENSO. Part I: Conceptual model. *Journal of the Atmospheric Sciences*, *54*(7), 811–829. [https://doi.org/10.1175/1520-0469\(1997\)054%3C;0811:AEORPF%3E;2.0.CO;2](https://doi.org/10.1175/1520-0469(1997)054%3C;0811:AEORPF%3E;2.0.CO;2)
- Kalnay, E., Kanamitsu, M., Kistler, R., Collins, W., Deaven, D., Gandin, L., et al. (1996). The NCEP/NCAR 40-year reanalysis project. *Bulletin of the American Meteorological Society*, *77*(3), 437–471. [https://doi.org/10.1175/1520-0477\(1996\)077%3C;0437:TNYRP%3E;2.0.CO;2](https://doi.org/10.1175/1520-0477(1996)077%3C;0437:TNYRP%3E;2.0.CO;2)
- Kay, J. E., Deser, C., Phillips, A., Mai, A., Hannay, C., Strand, G., et al. (2015). The Community Earth System Model (CESM) large ensemble project: A community resource for studying climate change in the presence of internal climate variability. *Bulletin of the American Meteorological Society*, *96*(8), 1333–1349. <https://doi.org/10.1175/BAMS-D-13-00255.1>
- Kim, J. W., & An, S. I. (2018). Origin of early-spring central Pacific warming as the 1982–1983 El Niño precursor. *International Journal of Climatology*, *38*(6), 2899–2906. <https://doi.org/10.1002/joc.5465>
- Kim, J. W., & An, S. I. (2019). Western North Pacific anticyclone change associated with the El Niño–Indian Ocean Dipole coupling. *International Journal of Climatology*, *39*(5), 2505–2521. <https://doi.org/10.1002/joc.5967>
- Levine, A. F., & McPhaden, M. J. (2016). How the July 2014 easterly wind burst gave the 2015–2016 El Niño a head start. *Geophysical Research Letters*, *43*, 6503–6510. <https://doi.org/10.1002/2016GL069204>
- Linkin, M. E., & Nigam, S. (2008). The North Pacific Oscillation–west Pacific teleconnection pattern: Mature-phase structure and winter impacts. *Journal of Climate*, *21*(9), 1979–1997. <https://doi.org/10.1175/2007JCLI2048.1>
- McPhaden, M. J., & Zhang, X. (2009). Asymmetry in zonal phase propagation of ENSO sea surface temperature anomalies. *Geophysical Research Letters*, *36*, L13703. <https://doi.org/10.1029/2009GL038774>
- Newman, M., Wittenberg, A. T., Cheng, L., Compo, G. P., & Smith, C. A. (2018). The extreme 2015/16 El Niño, in the context of historical climate variability and change. *Bulletin of the American Meteorological Society*, *99*(1), S16–S20. <https://doi.org/10.1175/BAMS-D-17-0116.1>
- Ohba, M., & Ueda, H. (2007). An impact of SST anomalies in the Indian Ocean in acceleration of the El Niño to La Niña transition. *Journal of the Meteorological Society of Japan Series II*, *85*(3), 335–348. <https://doi.org/10.2151/jmsj.85.335>
- Paek, H., Yu, J. Y., & Qian, C. (2017). Why were the 2015/2016 and 1997/1998 extreme El Niños different? *Geophysical Research Letters*, *44*, 1848–1856. <https://doi.org/10.1002/2016GL071515>
- Rayner, N. A. A., Parker, D. E., Horton, E. B., Folland, C. K., Alexander, L. V., Rowell, D. P., et al. (2003). Global analyses of sea surface temperature, sea ice, and night marine air temperature since the late nineteenth century. *Journal of Geophysical Research*, *108*(D14), 4407. <https://doi.org/10.1029/2002JD002670>
- Ren, H. L., Wang, R., Zhai, P., Ding, Y., & Lu, B. (2017). Upper-ocean dynamical features and prediction of the super El Niño in 2015/16: A comparison with the cases in 1982/83 and 1997/98. *Journal of Meteorological Research*, *31*(2), 278–294. <https://doi.org/10.1007/s13351-017-6194-3>
- Rogers, J. C. (1981). The North Pacific Oscillation. *Journal of Climatology*, *1*(1), 39–57. <https://doi.org/10.1002/joc.3370010106>
- Saji, N. H., Goswami, B. N., Vinayachandran, P. N., & Yamagata, T. (1999). A dipole mode in the tropical Indian Ocean. *Nature*, *401*(6751), 360–363. <https://doi.org/10.1038/43854>
- Santoso, A., McGregor, S., Jin, F. F., Cai, W., England, M. H., An, S. I., et al. (2013). Late-twentieth-century emergence of the El Niño propagation asymmetry and future projections. *Nature*, *504*(7478), 126–130. <https://doi.org/10.1038/nature12683>
- Santoso, A., McPhaden, M. J., & Cai, W. (2017). The defining characteristics of ENSO extremes and the strong 2015/2016 El Niño. *Reviews of Geophysics*, *55*, 1079–1129. <https://doi.org/10.1002/2017RG000560>
- Tseng, Y. H., Ding, R., & Huang, X. M. (2017). The warm Blob in the northeast Pacific—The bridge leading to the 2015/16 El Niño. *Environmental Research Letters*, *12*, 054019. <https://doi.org/10.1088/1748-9326/aa67c3>

- Vimont, D. J. (2010). Transient growth of thermodynamically coupled variations in the tropics under an equatorially symmetric mean state. *Journal of Climate*, *23*(21), 5771–5789. <https://doi.org/10.1175/2010JCLI3532.1>
- Watanabe, M., & Jin, F. F. (2002). Role of Indian Ocean warming in the development of Philippine Sea anticyclone during ENSO. *Geophysical Research Letters*, *29*(10), 1478. <https://doi.org/10.1029/2001GL014318>
- Webster, P. J., Moore, A. M., Loschnigg, J. P., & Leben, R. R. (1999). Coupled ocean–atmosphere dynamics in the Indian Ocean during 1997–98. *Nature*, *401*(6751), 356–360. <https://doi.org/10.1038/43848>
- Wu, X., Okumura, Y. M., & DiNezio, P. N. (2019). What controls the duration of El Niño and La Niña events? *Journal of Climate*, *32*(18), 5941–5965. <https://doi.org/10.1175/JCLI-D-18-0681.1>
- Xie, S. P., & Philander, S. G. H. (1994). A coupled ocean-atmosphere model of relevance to the ITCZ in the eastern Pacific. *Tellus A*, *46*(4), 340–350. <https://doi.org/10.3402/tellusa.v46i4.15484>
- Yeh, S. W., Cai, W., Min, S. K., McPhaden, M. J., Dommenges, D., Dewitte, B., et al. (2018). ENSO atmospheric teleconnections and their response to greenhouse gas forcing. *Reviews of Geophysics*, *56*, 185–206. <https://doi.org/10.1002/2017RG000568>
- Yu, J. Y., & Fang, S. W. (2018). The distinct contributions of the seasonal footprinting and charged-discharged mechanisms to ENSO complexity. *Geophysical Research Letters*, *45*, 6611–6618. <https://doi.org/10.1029/2018GL077664>
- Yu, J. Y., Kao, H. Y., & Lee, T. (2010). Subtropics-related interannual sea surface temperature variability in the central equatorial Pacific. *Journal of Climate*, *23*(11), 2869–2884. <https://doi.org/10.1175/2010JCLI3171.1>
- Yu, J. Y., & Kim, S. T. (2011). Relationships between extratropical sea level pressure variations and the central Pacific and eastern Pacific types of ENSO. *Journal of Climate*, *24*(3), 708–720. <https://doi.org/10.1175/2010JCLI3688.1>
- Yu, J. Y., & Lau, K. M. (2005). Contrasting Indian Ocean SST variability with and without ENSO influence: A coupled atmosphere-ocean GCM study. *Meteorology and Atmospheric Physics*, *90*(3–4), 179–191. <https://doi.org/10.1007/s00703-004-0094-7>



*Geophysical Research Letters*

Supporting Information for

**Understanding Re-intensified Multi-year El Niño Events**

Ji-Won Kim<sup>1</sup> and Jin-Yi Yu<sup>1</sup>

<sup>1</sup>Department of Earth System Science, University of California, Irvine, CA, USA

**Contents of this file**

Text S1

Table S1

Figures S1-S10

### **Text S1. Analyses with the 1300-year CCSM4 pre-industrial simulation**

Whether our results can be reproduced using other climate models is explored by repeating our analyses using a 1300-year CCSM4 pre-industrial simulation. A detailed description of CCSM4 is given by Gent et al. (2011) and the CCSM4 outputs can be found at <https://www.earthsystemgrid.org/dataset/ucar.cgd.cesm4.output.html>.

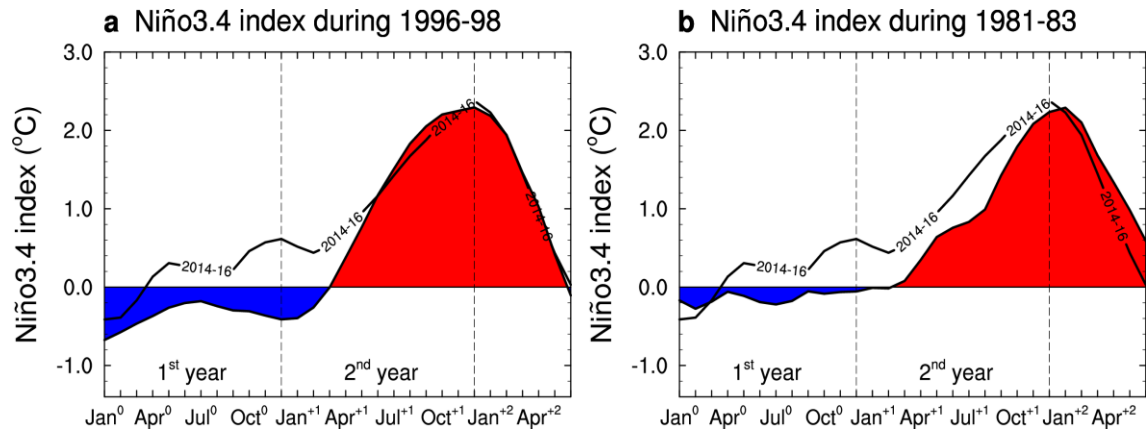
Figure S7 (which is the same as Fig. 1 except that it uses the CCSM4 simulation) shows similar evolutions of Niño3.4 index and equatorial Pacific SST anomalies among the three evolution groups of El Niño as those calculated from the CESM1 Pre-Industrial simulation (Fig. 1). Figure S7a indicates that a larger number of events have the succession (i.e., multi-year) characteristic than the transition characteristic in their evolutions. Figures S7b-f show clearly the three event groups with different evolution characteristics: succession and re-intensification event as Group1 (which is similar to the 2014-16 event), succession and lingering event as Group2, and transition event as Group3.

Figure S8 (which is the same as Fig. 2 except that it uses the CCSM4 simulation) shows that the 1<sup>st</sup>-year winter NPO as a cause for the succession characteristic, which is consistent with the analyses of the CESM1. As compared to the Group3 events, the atmospheric features in the Group1+2 events tend to have a stronger negative NPO phase with low pressure anomalies extending into the subtropical eastern Pacific. These stronger negative NPO-associated atmospheric features in Group1+2 (than Group3) favor to activate the WES feedback process; it then contributes to warm SST anomalies in the equatorial Pacific, and subsequently leads to a successive El Niño event.

Figure S9 (which is the same as Fig. 3 except that it uses the CCSM4 simulation) shows the 1<sup>st</sup>-year fall IOD as a cause for the re-intensification characteristic, which is consistent with the suggestion based on the analyses of CESM1. As compared to the Group2 events, Indian Ocean SSTs in the Group1 events exhibit anomalously warmer in the east and cooler in the west: the oceanic features of a negative IOD. These negative IOD-associated features (including atmospheric features) in Group1 eventually lead to westerly anomalies over the western Pacific as the season passes, thereby promoting to re-intensify warm SST anomalies in the equatorial Pacific in cooperation with the constructive effect from the negative NPO that assists the re-intensification.

**Table S1.** Statistical properties calculated from the three groups classified in this study. Values in parentheses in the 3<sup>rd</sup> row are for the positive IOD events. Note. NPO = North Pacific Oscillation, IOD = Indian Ocean Dipole

Classification	Evolution characteristics	Number of weak El Niño events	Percentage from total number of weak El Niño events	Mean of the extended winter NPO index	Number of negative NPO events	Percentage from total number of NPO events in the group	Mean of the extended fall IOD index	Number of negative IOD events	Percentage from total number of IOD events in the group
Group1	Succession and re-intensification	73	41%	-0.64	57	78%	-0.35	54	74%
Group2	Succession and lingering	33	19%	-0.32	22	67%	0.40	10 (23)	30% (70%)
Group3	Transition	72	40%	-0.04	38	53%	0.68	14	19%



**Figure S1.** Temporal evolutions of the Niño3.4 index from January<sup>0</sup> to June<sup>+2</sup> for the (a) 1996-98 and (b) 1981-83 events. The black curves in each panel indicate the 2014-16 event.

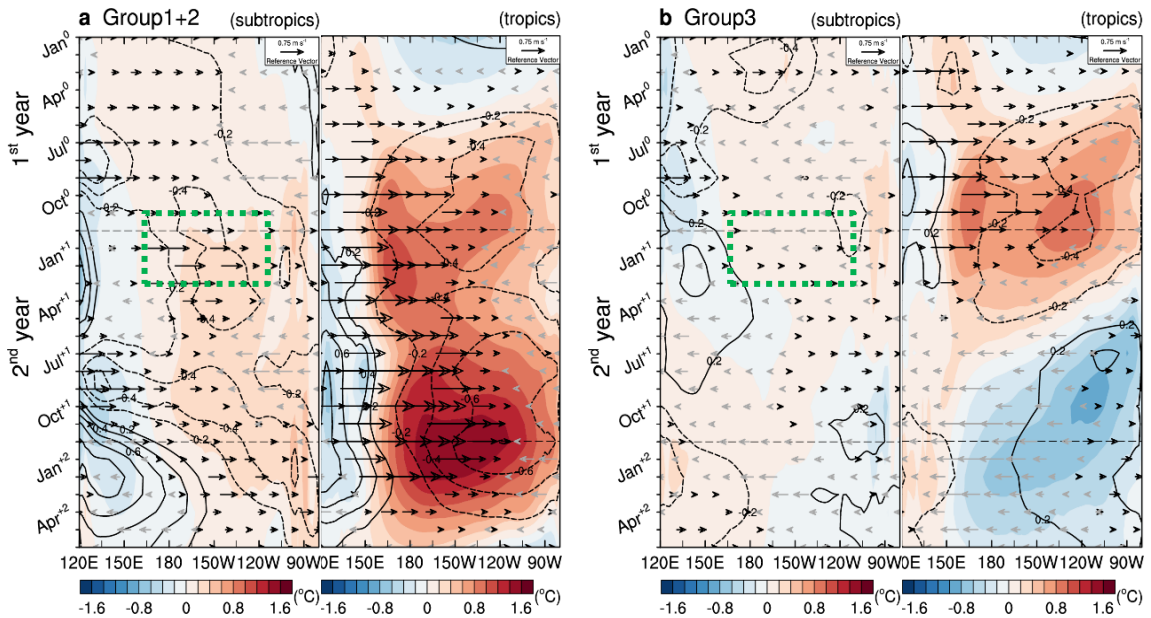


**Figure S2.** (a) Longitude–time plot of anomalous SST (shadings, in °C), sea level pressure (contour, in hPa; positive in solid and negative in dashed), and zonal wind (vector, in  $\text{m s}^{-1}$ ; westerlies in black and easterlies in gray) averaged over the subtropics between 10 and 20°N (left panel) and the tropics between 5°S and 5°N (right panel) for Group1+2. (b) is the same as (a) except for Group3. The green rectangle in the subtropics for Group1+2 reveals the area where negative NPO-related westerly anomalies exist, thereby inducing warm SSTAs and activating the WES feedback. No NPO-related westerly anomalies can be found in the same area for Group3.

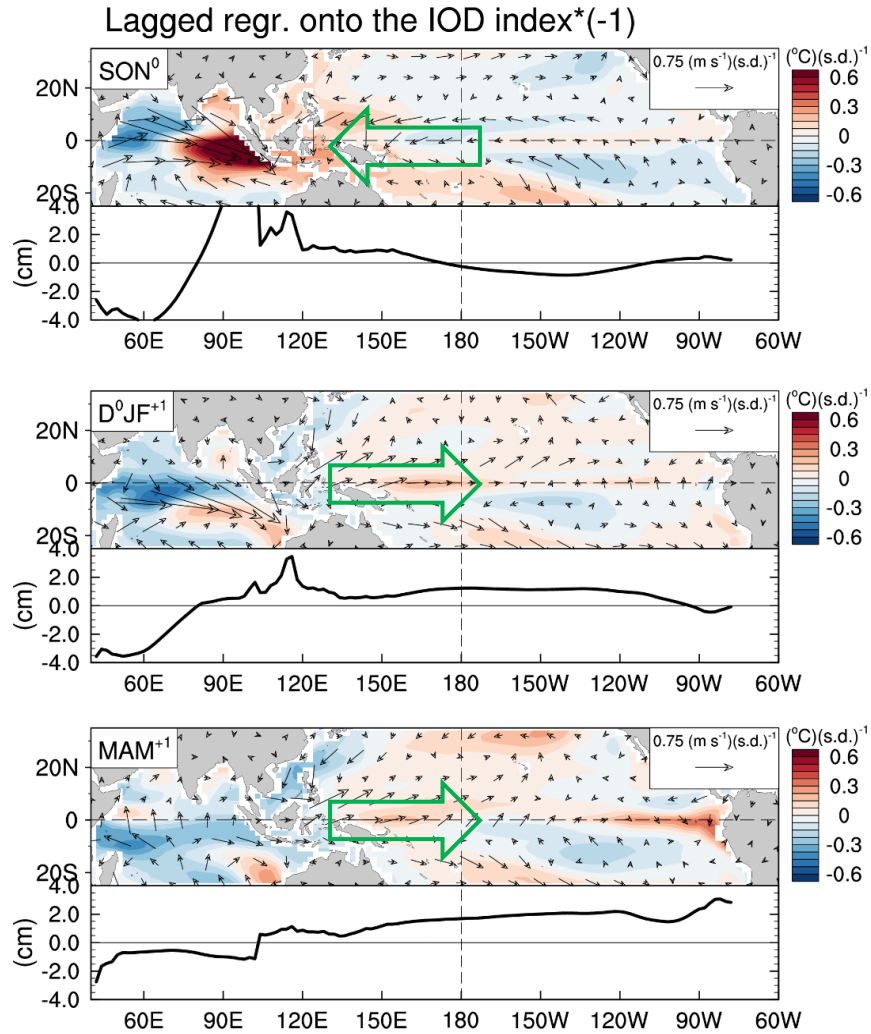


**Figure S3.** Lagged regression map of anomalous SST (shadings) and surface wind (vectors) and equatorially averaged ( $5^{\circ}\text{S}$ – $5^{\circ}\text{N}$ ) zonal structure of anomalous sea surface height (SSH; black curve) onto the inversed IOD index (multiplied by -1) during (top) fall (i.e., September–November;  $\text{SON}^0$ ), (middle) following winter (i.e., December–February;  $\text{D}^0\text{JF}^{+1}$ ), and (bottom) following spring (i.e., March–May;  $\text{MAM}^{+1}$ ). The variable SSH can be a proxy for upper ocean heat content in the tropical ocean. The impact of ENSO has been excluded by removing the linear regression with respect to the Niño3.4 index. The green arrows indicate the zonal directions of surface wind anomalies over the western Pacific, which change from easterly anomalies during fall to westerly anomalies during the following winter and spring.

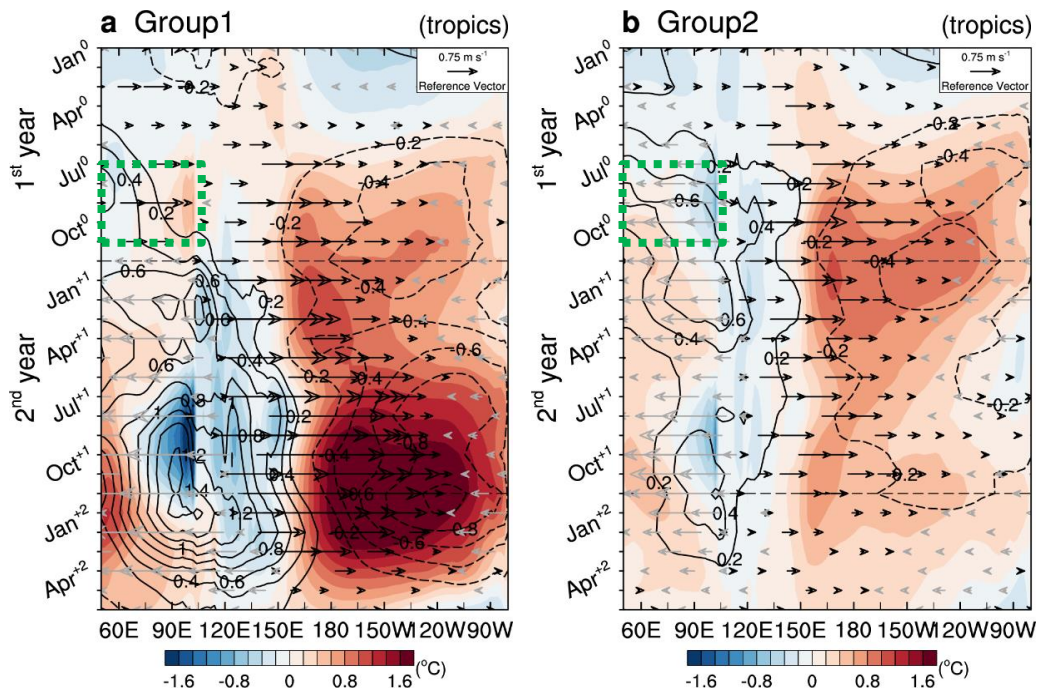


**Figure S4.** (a) Longitude–time plot of anomalous SST (shadings, in °C), sea level pressure (contour, in hPa; positive in solid and negative in dashed), and zonal wind (vector, in  $\text{m s}^{-1}$ ; westerlies in black and easterlies in gray) averaged over the tropics between 5°S and 5°N for Group1. (b) is the same as (a) except for Group2. The green rectangles indicate the opposite IOD phases in the Indian Ocean, with a negative IOD phase for Group1 but a positive IOD phase for Group2.

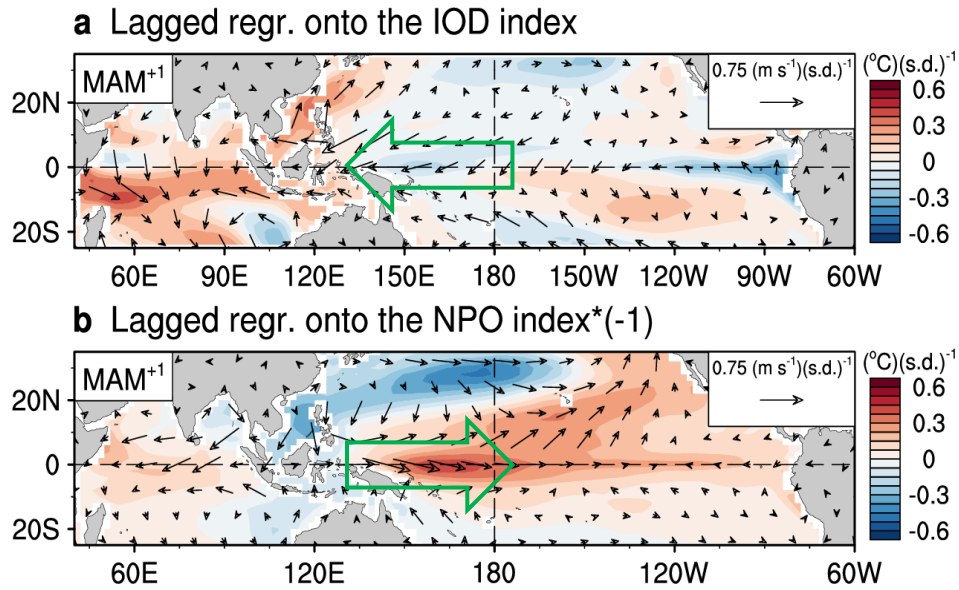


**Figure S5.** (a) Lagged regression map of anomalous SST (shadings) and surface wind (vectors) during spring (i.e., March-May;  $MAM^{+1}$ ) onto the preceding IOD index. (b) is same as (a) except onto the preceding NPO index multiplied by -1 to present the negative phase of NPO. The green arrows indicate the zonal directions of surface wind anomalies over the western Pacific, indicating the cancelling effect between the negative NPO and the positive IOD.

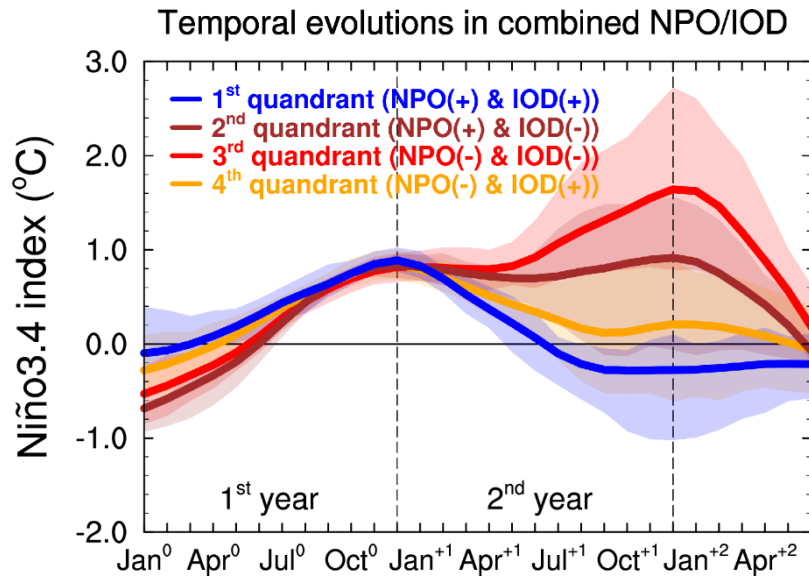


**Figure S6.** Temporal evolutions of the Niño3.4 index from January<sup>0</sup> to June<sup>+2</sup> for the events in the 1<sup>st</sup> quadrant (blue curve), 2<sup>nd</sup> quadrant (brown curve), 3<sup>rd</sup> quadrant (red curve), and 4<sup>th</sup> quadrant (orange curve) from Figure 4a (see the main context). The colored shadings indicate interquartile ranges between the 25<sup>th</sup> and 75<sup>th</sup> percentile for each quadrant.

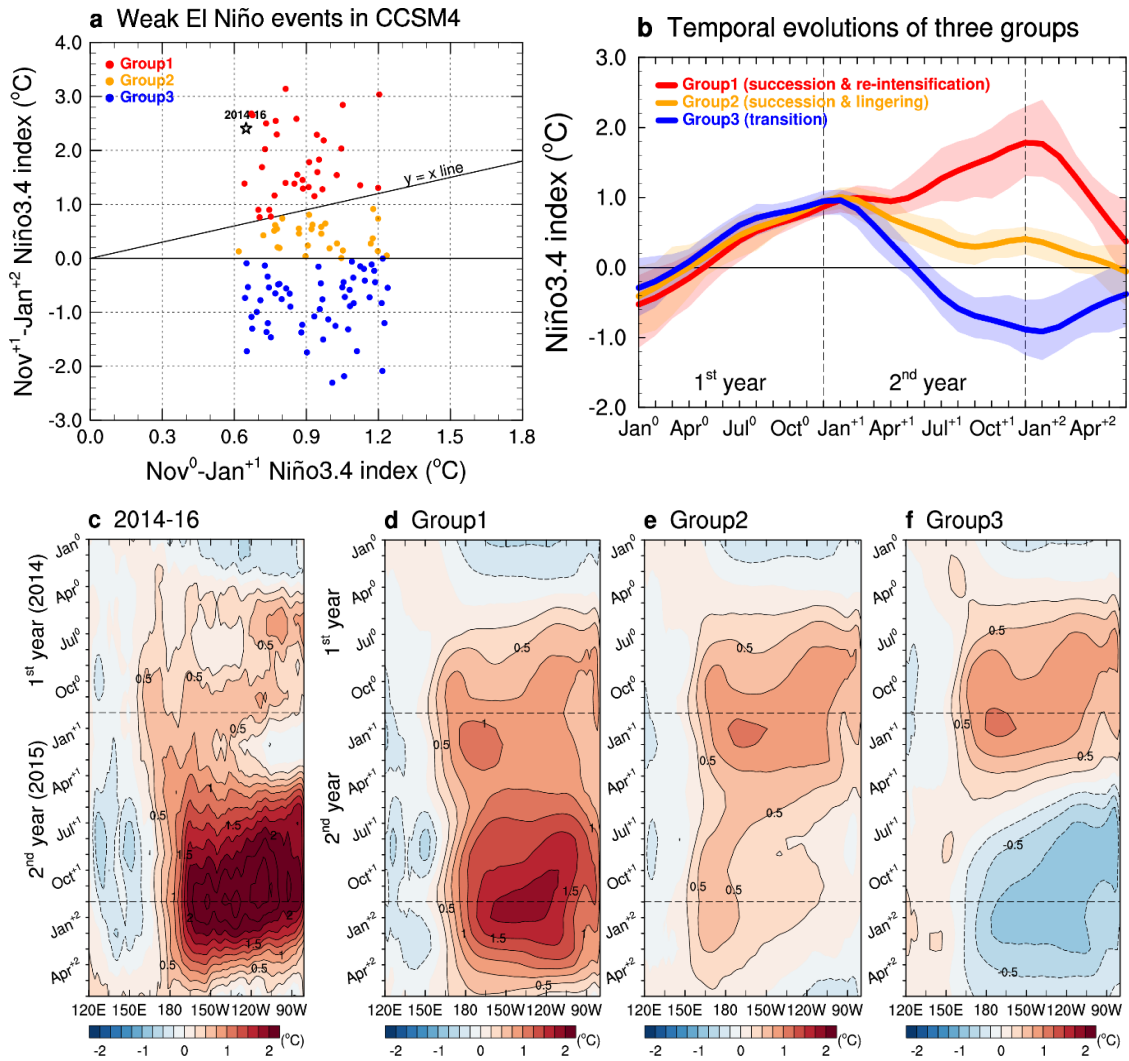


**Figure S7.** The same as Figure 1 except for the use of CCSM4

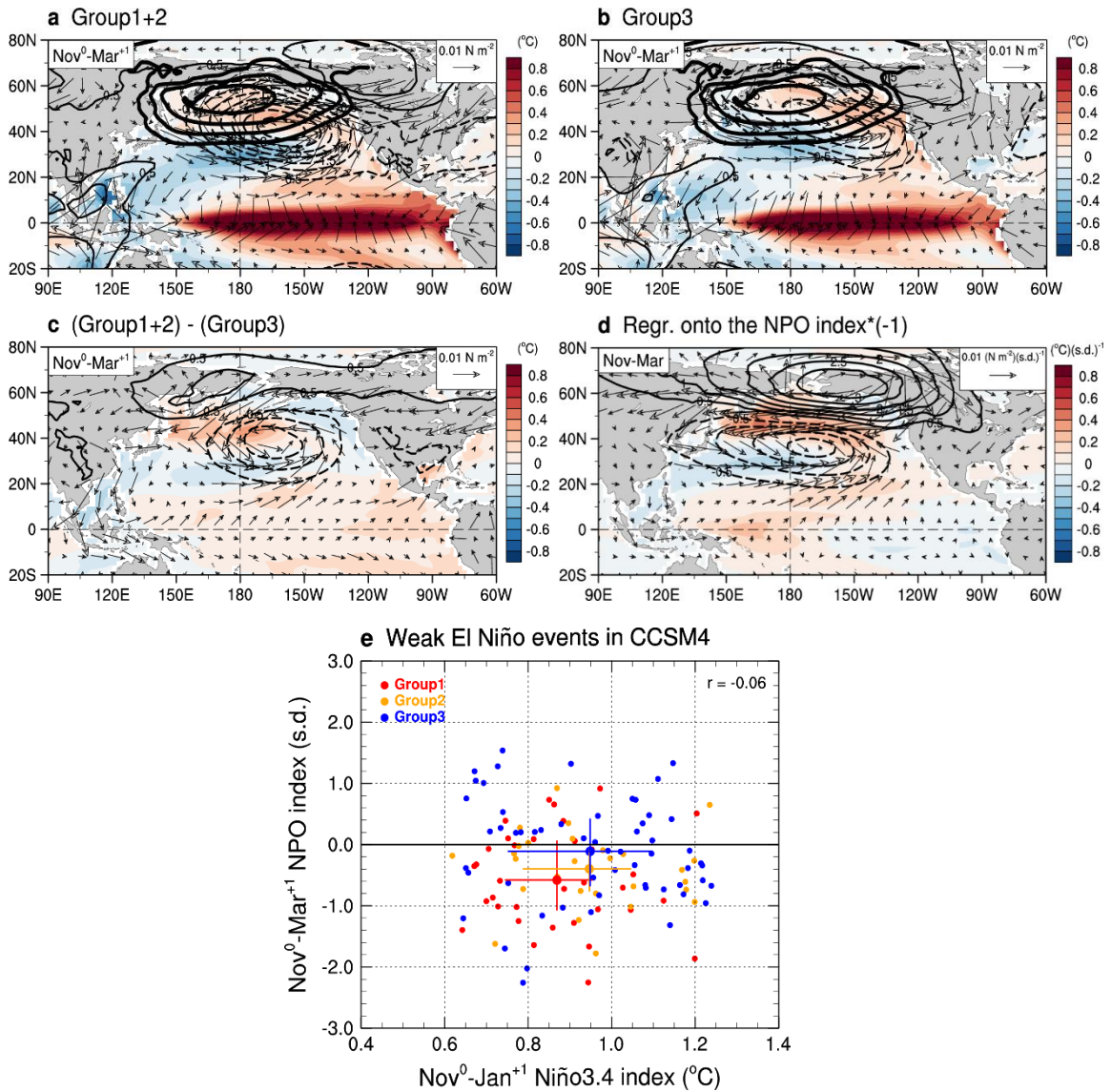


**Figure S8.** The same as Figure 2 except for the use of CCSM4. Wind stress (vectors; in  $\text{N m}^{-2}$ ) is alternatively used instead of surface wind.

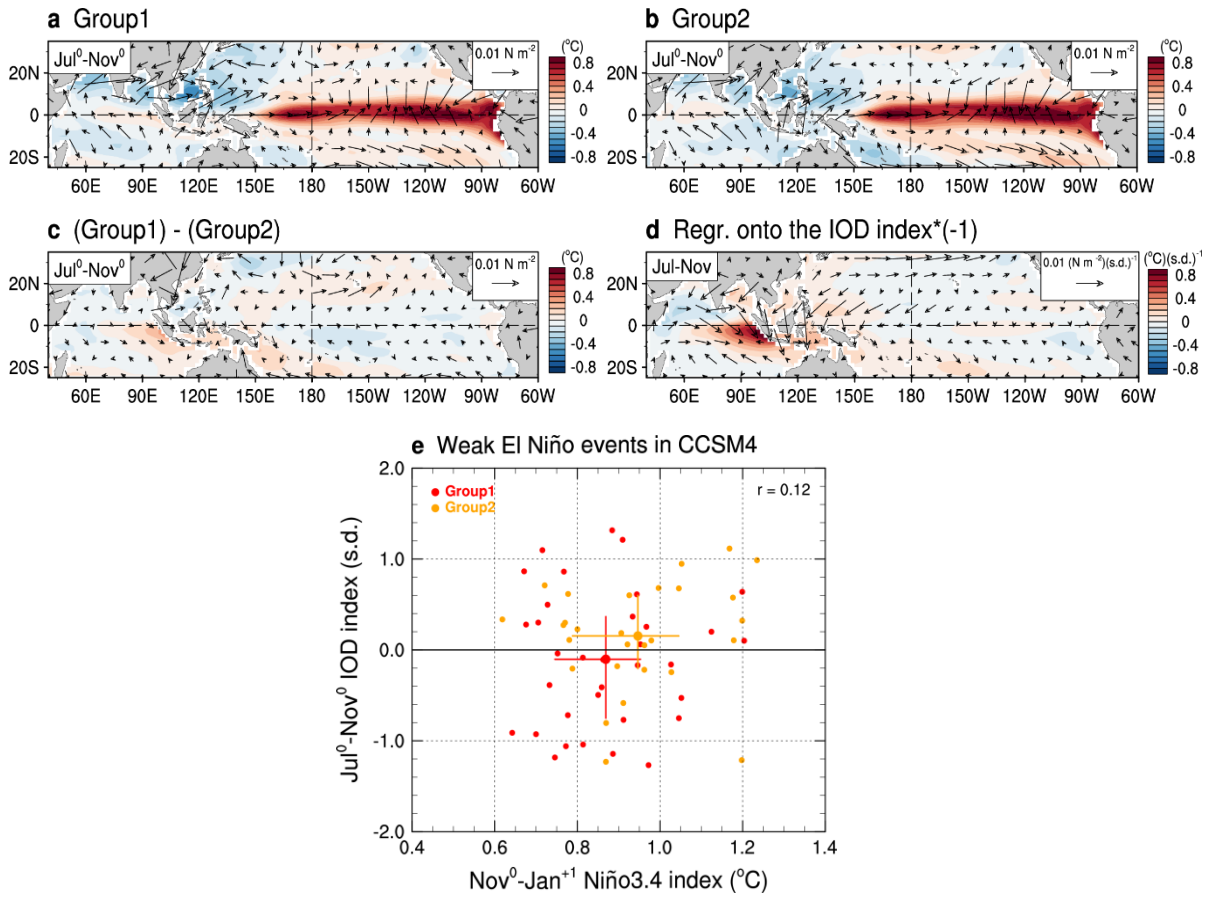


**Figure S9.** The same as Figure 3 except for the use of CCSM4. Wind stress (vectors; in  $\text{N m}^{-2}$ ) is alternatively used instead of surface wind.

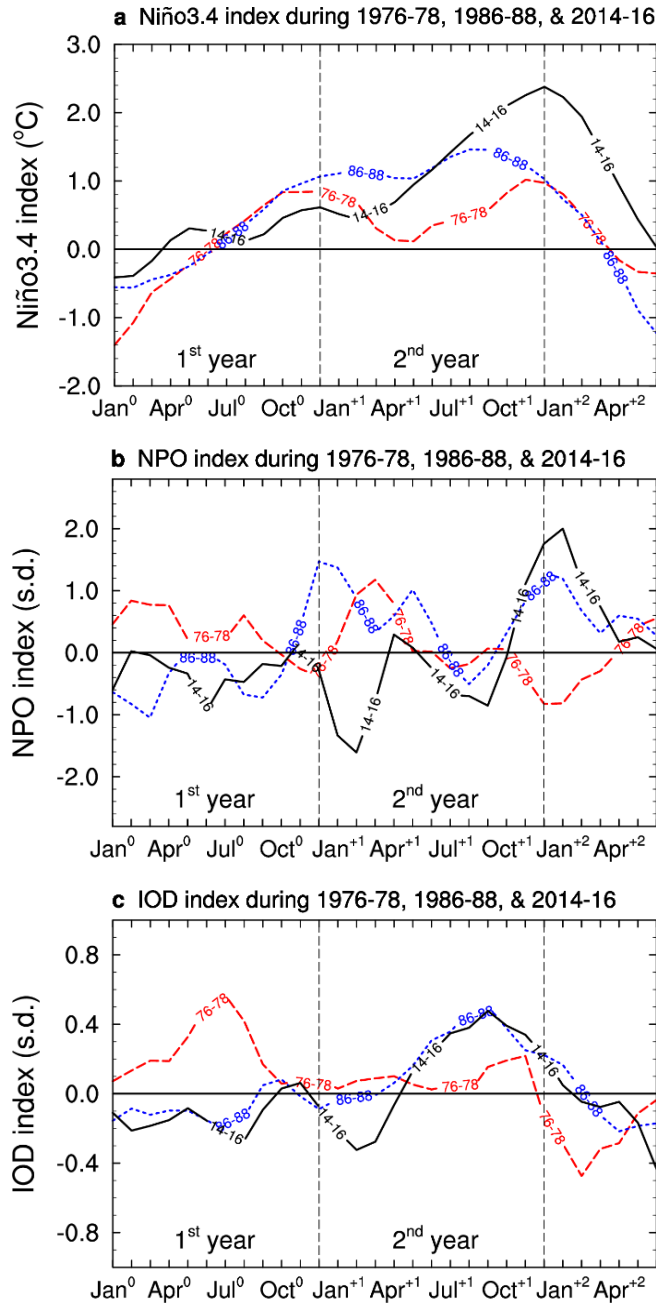


**Figure S10.** Temporal evolutions of the (a) Niño3.4, (b) NPO, and (c) IOD indices from January<sup>0</sup> to June<sup>+2</sup> for the 1976-78 (red, long-dashed), 1986-88 (blue, short-dashed), and 2014-16 (black, solid) events

## **Reference**

Gent, P. R., Danabasoglu, G., Donner, L. J., Holland, M. M., Hunke, E. C., Jayne, S. R., ... & Worley, P. H. (2011). The community climate system model version 4. *Journal of climate*, 24(19), 4973-4991.